Raju, Geet; Kyriakopoulos, Nikos; Timonen, Jaakko V.I.

Diversity of non-equilibrium patterns and emergence of activity in confined electrohydrodynamically driven liquids

Published in:
Science Advances

DOI:
10.1126/sciadv.abh1642

Published: 01/09/2021

Document Version
Publisher's PDF, also known as Version of record

PHYSICS

Diversity of non-equilibrium patterns and emergence of activity in confined electrohydrodynamically driven liquids

Geet Raju, Nikos Kyriakopoulos, Jaakko V. I. Timonen*

Spontaneous emergence of organized states in materials driven by non-equilibrium conditions is of notable fundamental and technological interest. In many cases, the states are complex, and their emergence is challenging to predict. Here, we show that an unexpectedly diverse collection of dissipative organized states emerges in a simple system of two liquids under planar confinement when driven by electrohydrodynamic shearing. At low shearing, a symmetry breaking at the liquid-liquid interface leads to a one-dimensional corrugation pattern. At slightly stronger shearing, topological changes give raise to the emergence of Quincke rolling filaments, filament networks, and two-dimensional bicontinuous fluidic lattices. At strong shearing, the system transitions into dissipating polygonal, toroidal, and active droplets that form dilute gas-like states at low densities and complex active emulsions at higher densities. The diversity of the observed dissipative organized states is exceptional, pointing toward non-equilibrium optical devices and new avenues in several fields of research.

INTRODUCTION

Spontaneous organization of matter into complex structures under non-equilibrium conditions is of both major fundamental and technological interest across disciplines, from physics to biology (*1*–*3*). In the context of physics, it is often manifested by symmetry breaking and the emergence of unexpected patterns in continuum systems driven by external fields (*1*) and as structural organization of externally driven (*4*) and self-propulsive (active) particles (*5*). In (bio) chemical systems, it is often seen as active gelation (*6*) of both biological (*7*) and synthetic molecules (*8*–*10*). In biological systems, it is manifested, for example, by collective motion of microscopic (*3*) and macroscopic (*11*, *12*) organisms. Although progress has been made toward theoretical descriptions (*1*, *3*, *13*, *14*), predicting the systems and required non-equilibrium conditions that lead to the emergence of complex structures still remains a challenge.

There is a rich literature on using electrohydrodynamics (EHD) (*15*) to drive agent motion, be it solid particle rotation and translation or three-dimensional (3D) liquid droplet rotation and deformation. Major advances have been made toward understanding the properties of such systems regarding their interactions and collective behavior, in the case of solid spheres (*16*–*19*), and their deformation and splitting, in the case of liquid droplets (*20*–*27*). Even so, there are still many areas left unexplored in the electrohydrodynamically driven systems. For example, active particles driven by the Quincke electrorotation mechanism have been symmetric (spherical) solid particles (*16*–*18*), although liquid droplets could allow particles with externally controlled shape and interactions that would be especially interesting because of the predicted effects of lower symmetry on their collective behavior (*28*). In addition, while some examples of confinement have been explored in the case of solid particles, the geometry has never been confining in the case of freely moving liquid droplets between nonwetting surfaces that is known to lead to a suitable environment for droplet self-assembly (*29*).

Department of Applied Physics, Aalto University School of Science, P.O. Box 15100, Espoo FI-02150, Finland.
*Corresponding author. Email: jaakko.timonen@aalto.fi

Here, we confine a simple biphasic liquid system between two nonwetting surfaces, thus forcing quasi-2D behavior. The confinement, along with the deformability of the liquid drops and their material properties, leads to strong deformation of the interface when an external electric field is introduced. The deformation is driven by nontrivial EHD flows and shearing of the interface. As a result, an unexpected diversity of complex, non-equilibrium fluidic patterns and fluidic objects of various shapes emerge (Fig. 1 and movie S1). Our system relies on a novel combination of two immiscible oils: fluorinated perfluoropolyether (PFPE) and a dodecane (DD) solution containing 75 or 150 mM bis(2-ethylhexyl) sulfosuccinate sodium salt [aerosol OT (AOT)], confined between two parallel glass slides coated with indium tin oxide (ITO) and separated by a distance h (Fig. 1A and fig. S1), between 36 and 68 μm (tables S1 and S2).

The combination of oils used has three critical properties. First, the oils have a large conductivity contrast ($\sigma_{PFPE} \approx 10^{-17}$ S/m $\ll \sigma_{AOT/DD} \approx 10^{-8}$ S/m; table S3) that is required for driving strong electrohydrodynamic flows near the oil-oil interface (*15*). Second, the contact angle θ of the essentially insulating PFPE on the ITO surfaces (used as electrodes) surrounded by the AOT/DD phase is close to ideal nonwetting, i.e., $\theta \approx 180°$. Third, the adhesion of the PFPE phase on the ITO is negligible. The latter two properties allow the PFPE phase to form highly mobile slab-shaped droplets with semicircular oil-oil interface when confined in a planar cell between two parallel ITO-coated electrodes in thermodynamic equilibrium (Fig. 1A) (*30*). We drive this interface out of the equilibrium by applying a voltage U between the ITO-coated electrodes, resulting in electric field $E_0 = U/h$. This leads to a dynamic charge density at the oil-oil interface that experiences a Coulombic destabilizing (shearing) force (Fig. 1A) (*15*) that is counteracted by the interfacial tension $\gamma \approx 8$ mN/m (see Materials and Methods) (*30*). At suitable balance between these forces, the interface (Fig. 1B) goes through numerous unexpected symmetry breakings and changes in topology that lead to a notable variety of non-equilibrium patterns and active objects (Fig. 1C): dissipative quasi-1D patterns at the oil-oil interface, Quincke rolling liquid filaments and dissipative filament networks

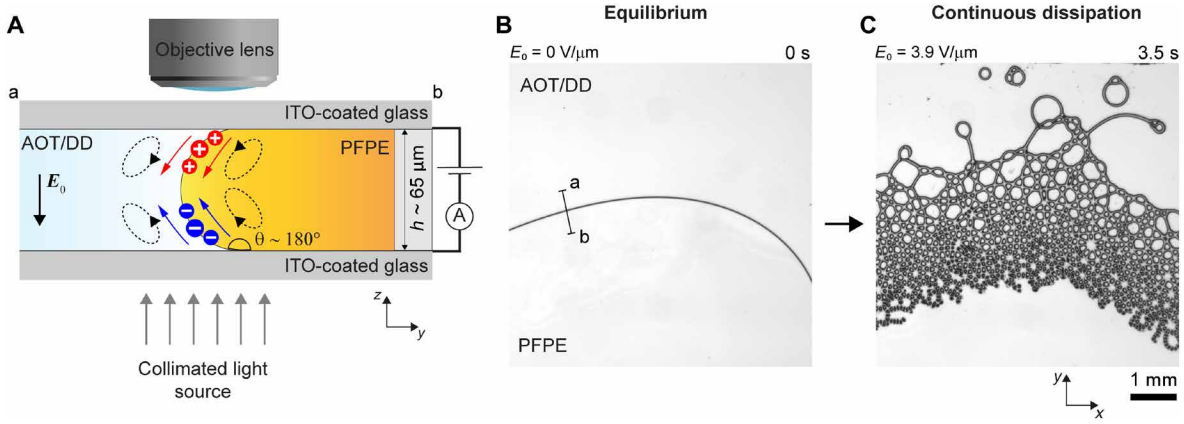

Fig. 1. Emergence of diverse non-equilibrium fluidic structures in a simple electrohydrodynamically driven planar system. (**A**) Scheme of the cross section of a PFPE drop (orange) surrounded by a mixture of DD and AOT (AOT/DD) (light blue) between two ITO-coated glass slides. Red and blue arrows indicate Coulombic force and flow direction at the oil-oil interface for positive (red) and negative (blue) interfacial charges. Dashed black loops and arrows indicate resulting flow fields outside the interface. The same color scheme and notation are used throughout the article. (**B**) An image of the oil-oil interface in equilibrium state observed in the experiments. (**C**) An image of a typical non-equilibrium state comprising active filaments, random filament networks and ordered 2D fluidic lattices, and active and self-propulsive electrohydrodynamically sculpted droplets and active emulsions. Photo credit: G. Raju, Aalto University.

and lattices, and active self-propulsive and electrohydrodynamically sculpted droplets.

RESULTS

Electrohydrodynamically driven deformation, instability, and pattern formation along the liquid-liquid interface

When the electrohydrodynamic driving is weak (small electric field magnitudes), the interfacial tension largely keeps the oil-oil interface close to the equilibrium shape. The only small indication of the electrohydrodynamic shearing comes from the minute reshaping of the interface upon increasing the electric field. This is observed in our microscopy experiments (see Materials and Methods) as changes in the dark band corresponding to the oil-oil interface created by the refraction of light from the curved interface (Fig. 2A and fig. S2A). When the voltage is increased, the width of the dark band gradually increases from the equilibrium value $w_0 \approx h/2$ (as expected for semicircular interface) as $w = w_0(1 + AE_0^{\alpha})$, where $\alpha \approx 2.6$ (Fig. 2B and fig. S2, B and C). The widening is driven by the antisymmetric charging of the oil-oil interface with respect to the midplane of the cell and the resulting symmetric electrohydrodynamic shearing of the interface toward the midplane and the apex of the interface (Fig. 2A). This is analogous to the Taylor flow pattern observed in freely suspended, nonconfined spherical droplets, which leads to axisymmetric droplet flattening, known since the 1960s (*31*). The widening of the interface is reversible, and the oil-oil interface returns to the equilibrium state when the electric field is turned off (fig. S2D).

At slightly larger electric fields above a threshold value $E_c \approx 4$ V/μm, the shear-widened interface (Fig. 2A) is no longer stable and thus undergoes a spontaneous symmetry breaking. This leads to the population of the oil-oil interface with periodically alternating peaks and valleys (Fig. 2D and movie S2) in a pattern reminiscent of Faraday waves (*32*) and the Rosensweig pattern (*33*) but now in one dimension. If the applied field is only slightly above the E_c (i.e., close to the threshold), then the instability and pattern formation take place in a few tens of milliseconds in two distinct steps (Fig. 2C): First, the interface elongates (taking ca. 1 to 2 ms), followed by a short quiescent time and the spontaneous symmetry breaking (taking ca. 5 ms). If the applied field is far above the threshold E_c, then the two processes are not well separated in time. The steady-state spacing between the peaks, $\lambda_{pp} \approx 65$ μm, is close to the cell height $h = 68 \pm 0.6$ μm (Fig. 2D). However, careful microscopic observation shows that the peaks appear in pairs with alternating light and dark valleys between them (Fig. 2D), indicating that the true periodicity is $\lambda \approx 2h$. This observation is reinforced by the intensity profile analysis along lines normal to the interface at neighboring peak and valley positions (Fig. 2E), showing different profiles for the valleys. When the imaging system is focused at the midplane of the cell, the peaks appear to be in focus, while the valleys are out of focus. This suggests that the edges of the valleys are alternating above and below the midplane of the cell (Fig. 2D). In addition, experiments using high-speed microscopic imaging show that tracer particles (microscopic PFPE droplets) circulate near every second valley in a plane perpendicular to the interface, completing a full loop in $\tau \approx 8$ ms (movie S2). These observations point toward a mechanistic picture, wherein the symmetric Taylor-like electrohydrodynamic flow is spontaneously broken and the system adopts a state similar to the rotational Quincke flow (*34*), only with a periodically alternating direction of rotation along the oil-oil interface (Fig. 2, E and F).

Emergence of Quincke rolling filaments and bicontinuous dissipative fluidic lattices

Further increasing the strength of electrohydrodynamic driving leads to the emergence of another class of patterns and structures that are no longer spatially restricted to the vicinity of the original oil-oil interface. Rather, the forming patterns and structures emerge from the oil-oil interface (Fig. 3A) and propagate to fill the whole sample cell (movie S3). The formation of these patterns and structures is enabled by topological changes in the system, wherein the electrohydrodynamic shearing punches holes through the slab-like PFPE drop (Fig. 3B and movie S4). The holes grow rapidly, and if the expansion of the holes is unrestricted, then rolling filaments are produced (Fig. 3, C to G).

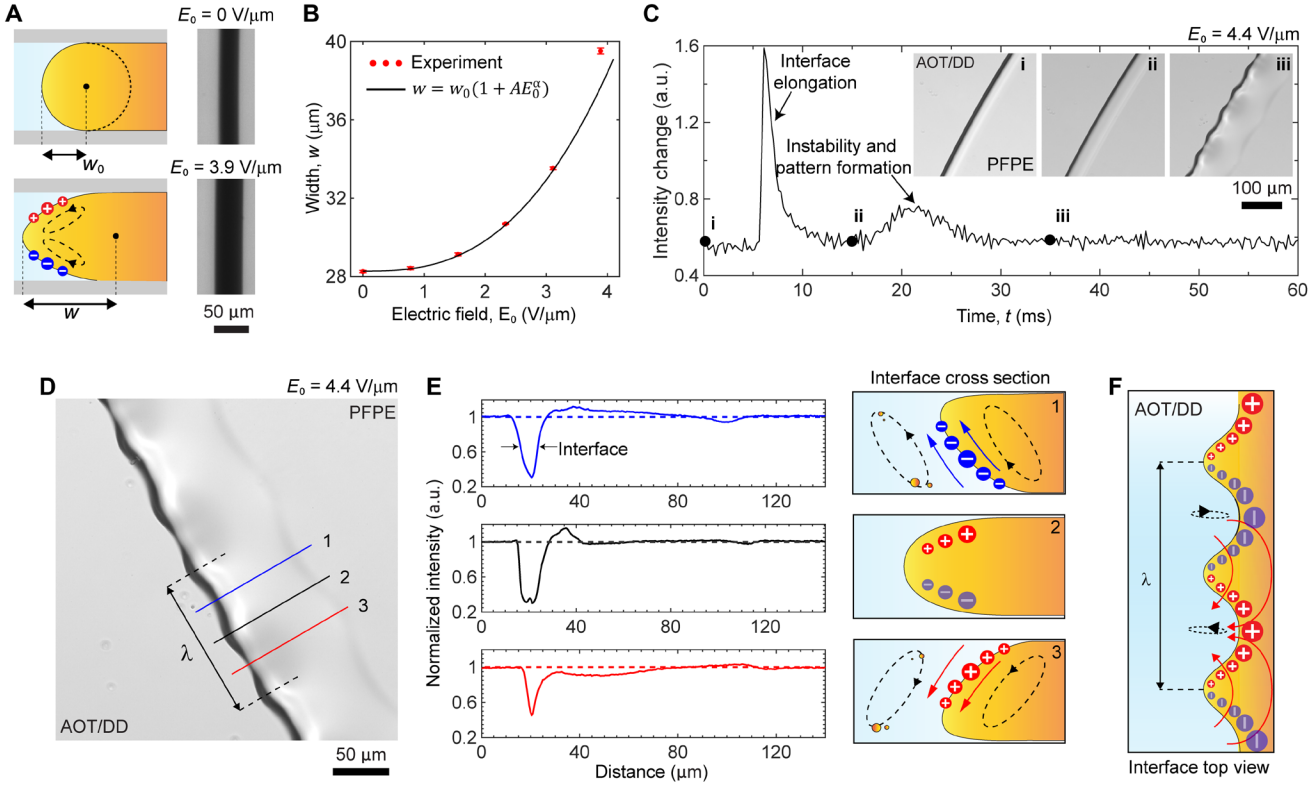

Fig. 2. Electrohydrodynamically driven reshaping of the oil-oil interface and emergence of dissipative interfacial patterns. (**A**) Schemes and images of the oil-oil interface, with and without an applied field. (**B**) Width (FWHM) of the oil-oil interface as a function of electric field magnitude strength. The solid line denotes the fit $w = w_0(1 + AE_0^{\alpha})$, with $w_0 = 28.25$, $A = 0.0097$, and $a = 2.6$. The rightmost experimental point was ignored in the fit, as the corrugation pattern starts appearing near that field magnitude. (**C**) Change in image intensity between consecutive frames as a function of time $\Delta I(t) = \sum\sum |I_{ij}(t + \Delta t) - I_{ij}(t)|$, where $I_{ij}(t)$ is the matrix of pixel intensities in the frame recorded at time t when an electric field above E_c is applied (movie S2). Insets show images before voltage is applied, after the interface has elongated, and after the elongated interface has developed the pattern. (**D**) An image showing the steady-state dissipative interfacial pattern. (**E**) Normalized intensity of the interfacial patterns along the lines marked in (D) and the corresponding cross-sectional schemes at the interface. (**F**) Top-view scheme of the interfacial pattern. a.u., arbitrary units.

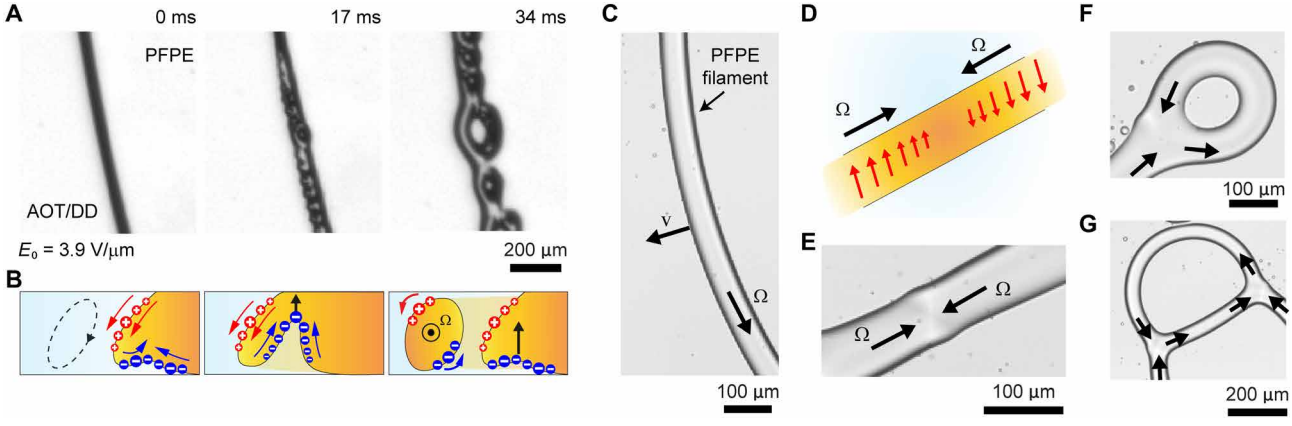

Fig. 3. Emergence of active filaments and filament networks. (**A**) Images of the oil-oil interface at zero field and upon application of voltage $E_0 > E_c$ (movie S3). (**B**) Scheme illustrating the mechanism for emergence of active filaments. (**C**) Image of a simple active filament with rotational (Quincke) flow resulting in a translational velocity $v \approx 3.5$ mm/s (movie S5). (**D**) Scheme of an active filament illustrating the emergence of frustration-induced bumps. (**E**) A corresponding image of an active filament with said bump. (**F** and **G**) Images of typical filament junctions with frustration-induced bumps indicated with black arrows (movie S6).

The observed filaments (Fig. 3, C to G) are quasi–self-propulsive objects with a diameter close to the cell height. Tracer particles circulate rapidly around the filaments, typically one rotation in $\tau \approx 1$ ms (movie S5). This suggests that the filaments are in a state of Quincke electrorotation, where the electric dipole on the filament is spontaneously tilted with respect to the electric field, thus resulting in continuous electric torque on the filament that is balanced by the viscous torque (*34*). We note that Quincke rotation alone is not

sufficient to create propulsion but requires also an asymmetric environment around the rotating object. For example, in the case of solid particles propelled by the Quincke mechanism (*16*–*18*), this asymmetry comes from the glass slide on which the particles rest on. In our case, the gravitational force slightly flattens the PFPE filament between the ITO electrodes, thus breaking the symmetry and resulting in the translational motion of the filaments at slow speeds as expected (*34*, *35*). The active filaments also form complicated filament networks by looping back onto themselves or coupling with other filaments (Fig. 3, F and G, and movie S6). These structures exhibit frustration in the rotational flow direction at the junctions, which leads to the formation of small bumps (Fig. 3, E to G) and optical contrast at the locations where the tangential flows vanish. This is consistent with the conclusion regarding the flow fields near the peaks at the oil-oil interface at lower voltages (Fig. 2, E and F).

On the other hand, if the hole growth is limited, then dissipative ordered fluidic lattices appear (Fig. 4). The observed dissipative fluidic lattices (Fig. 4, A and E) are quasi-static, bicontinuous, and periodic fluidic structures with lattice constants on the same order of magnitude as the cell height. Dissipative lattices form via the repeated punching of holes through the PFPE droplet under conditions where the hole growth is highly restricted (Fig. 4, A and B). Two lattices were observed to be especially frequent and stable: a trihexagonal lattice (Kagome lattice; Fig. 4, E and F, and movie S7) and a double-square lattice (Fig. 4, A to D, and movie S8). In both lattice types, the neighboring lattice sites (pockets of AOT/DD in the PFPE slab) exhibit liquid flow in opposing directions, either upward or downward (Fig. 4B). This is seen directly as circulatory flows between neighboring lattice sites in tracer particle trajectories (Fig. 4C and movie S8), which again suggests a Quincke-like state of flow (*34*), but now in the form of a periodic fluidic lattice. It appears that only some lattice symmetries are allowed due to the requirement of neighboring sites to flow in opposite directions. This is in agreement with both the two observed lattices and in the lack of observation of the typical simple hexagonal tiling.

The fluidic filaments and lattices are reversible: When the voltage is turned off, the structures relax quickly back to unstructured pancake-shaped liquid droplets that coalesce to form larger volumes, driven by the minimization of the interfacial energy (movie S9). The complete separation back to two large fluidic volumes can be realized conveniently by tilting the sample along the gravity to drive the denser PFPE toward one end of the sample cell.

Electrohydrodynamically driven polygonal, toroidal, and active droplets and emulsions

In addition to bicontinuous active filaments and dissipative lattices (Figs. 3 and 4), discontinuous active droplets also emerge in the system (Fig. 5). Active droplets are most often formed from the active filaments in a process reminiscent of the Plateau-Rayleigh instability (*36*), but with a fast rotating liquid filament (Fig. 5A and movie S10). A single instability event along a filament leads to pinching of microdroplets with diameters d much smaller than the cell height h (Fig. 5, A and B). If two instability events take place along a single filament, then larger droplets are formed (Fig. 5, A and B, and fig. S3A). The small droplets ($d < h$) are not substantially deformed by confinement or electrohydrodynamic shearing and spontaneously become self-propulsive with translational velocities up to millimeters per second, forming a disordered gas-like state at low densities

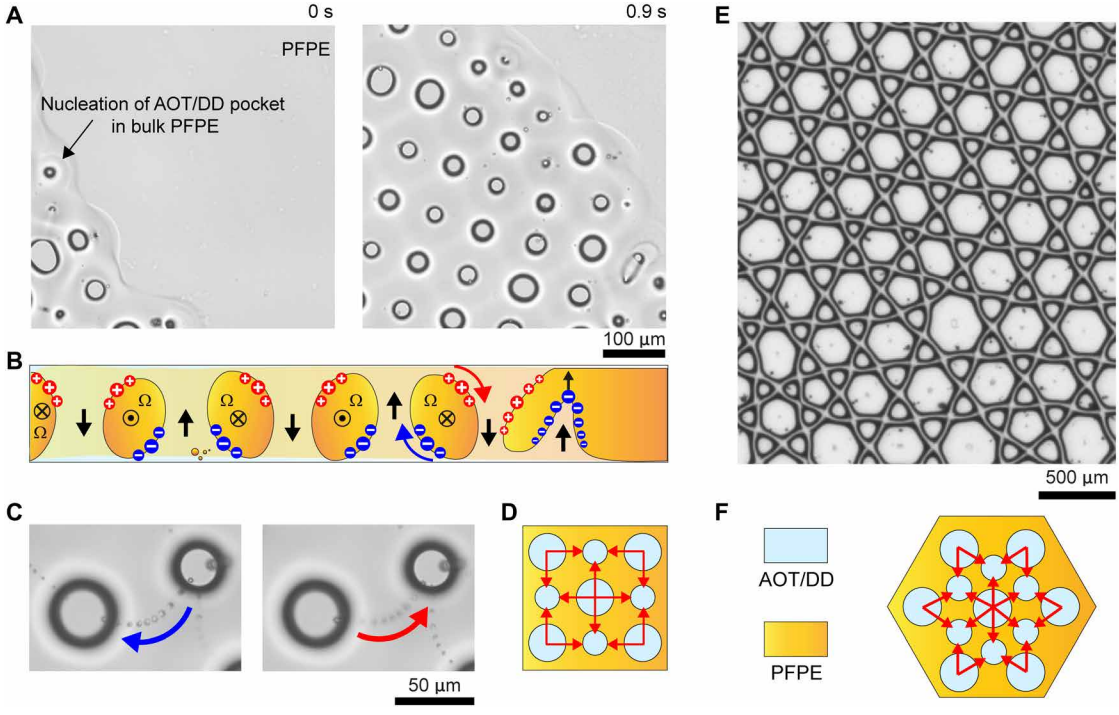

Fig. 4. Non-equilibrium fluidic lattices. (**A**) Images of nucleation and propagation of pockets of AOT/DD away from the oil-oil interface upon application of voltage $E_0 > E_c$ (movie S4) leading to the emergence of a square lattice. (**B**) Corresponding scheme illustrating the mechanism. (**C**) Overlaid images showing a tracer particle moving between two neighboring pockets in the square lattice (movie S8). (**D**) Scheme of the square lattice type. (**E** and **F**) Experimental image and corresponding scheme of an electrohydrodynamically driven Kagome lattice (movie S7).

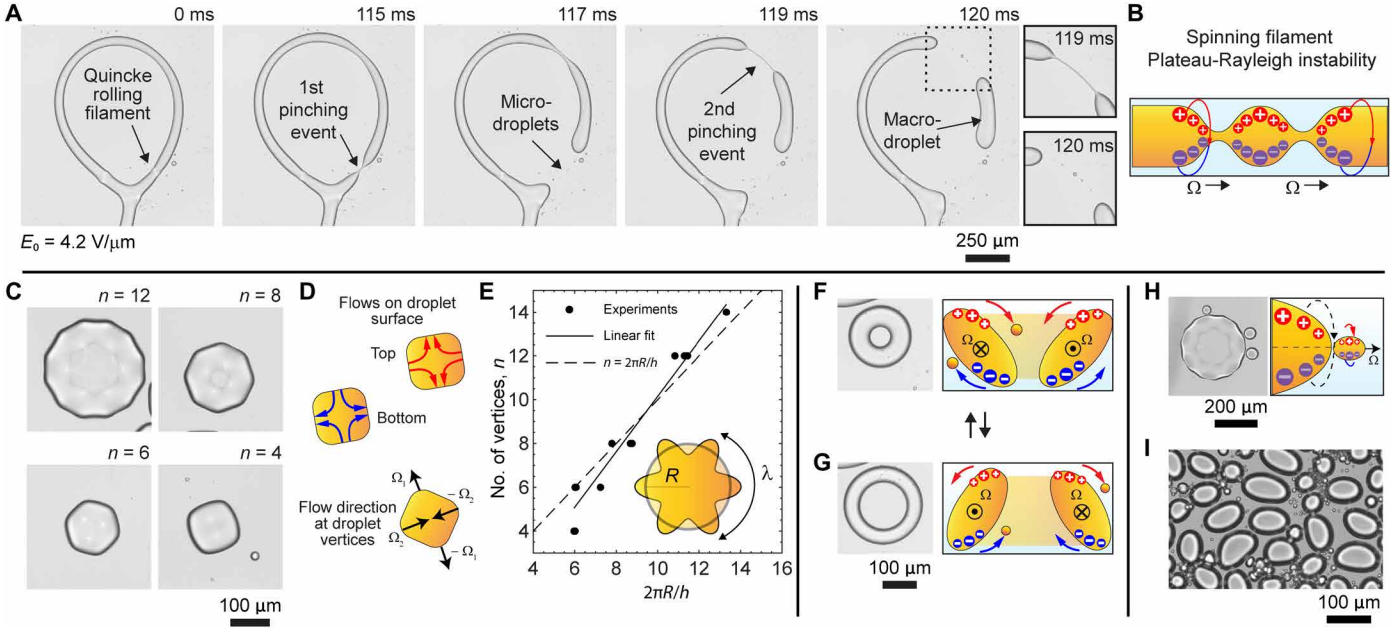

Fig. 5. Emergence and dynamics of active liquid droplets, self-assemblies, and emulsions. (**A**) Time series of microscopy images showing formation of active droplets (movie S10). (**B**) Scheme of spinning filament Plateau-Rayleigh instability in a rotating liquid filament. (**C**) Images of typical polygonal droplets. (**D**) Scheme showing flow fields and rotational directions for the square droplet ($n = 4$). (**E**) Plot of the number of vertices on droplets versus their circumference at $E_0 = 0$ scaled by the cell height. Inset: Scheme of a droplet ($n = 6$) with exaggerated geometry, highlighting the relationship between radius R and pattern wavelength λ. (**F** and **G**) Images of two toroids with opposing directions of rotation and their corresponding schemes. (**H**) Images and schemes of droplet self-assemblies. (**I**) An image of a high-concentration emulsion of active droplets with suppressed coalescence (movie S19).

(movie S11). If the driving electric field is turned off and back on, then the directions of the droplets' motions are reset and randomly chosen again (movie S11 and fig. S4). This suggests that the propulsion mechanism is similar to the solid active Quincke rollers studied frequently (*16*–*18*). Observations of the tracer particle motion near an active PFPE droplet show circulation of the tracer particles around the axis of the droplet that is perpendicular to the direction of motion (movie S12), providing further evidence that the mechanism for the propulsion is indeed Quincke rotation. At higher fields, droplet clustering into dimers and trimers was observed (movie S13).

The larger droplets ($d > h$), on the other hand, are substantially deformed by confinement and electrohydrodynamic flows, resulting in unexpected droplet shapes. For example, the large droplets can adopt polygonal shapes with up to $n = 14$ vertices (Fig. 5C and fig. S5, A and B). The number of vertices is always even, and the droplets appear almost stationary (nonmoving and non–shape shifting). However, as in the steady-state, interfacial patterns at low electrohydrodynamic driving (Fig. 2D), the polygonal droplets experience continuous strong internal electrohydrodynamic flows (movie S14). In addition, the vertices of the polygons seem to correspond to the peaks of the interfacial patterns (Fig. 2F) and the bumps at the filament-filament junctions (Fig. 3, D and E) where flow velocities vanish (Fig. 5D). Similarly, the edges of the polygons seem to correspond to the valleys of the interfacial patterns (Fig. 2D). Thus, a polygonal droplet with n vertices has an apparent n-fold rotational symmetry, but when internal flows are taken into account, it has an $n/2$-fold rotational symmetry (fig. S5B), explaining why only even-sided polygons were observed. Peak-valley pairs appear on the circumference of a droplet, created by the mechanism described previously for the straight interface (Fig. 2). The neighboring peaks have a spacing of $\lambda/2$, and they wrap around the circumference of the droplet; thus, the length of the circumference $2\pi R$ dictates how many peaks can fit into it, i.e., $n \approx 4\pi R/\lambda$, where n has to be an integer and $\lambda \approx 2h$ (Fig. 5E, inset). This is in agreement with experimental observations (Fig. 5E). There also appears to be a critical size ($n_c \approx 14$ for the studied system) beyond which the polygonal droplets are no longer stable (fig. S3B and movie S15).

In addition to the polygonal droplets, another peculiar nonequilibrium droplet type is the active toroid made of a looped PFPE filament (Fig. 5, F and G, and movie S16). Active toroids can rotate inward or outward, resulting in slightly different apparent sizes (Fig. 5, F and G). This is in agreement with the observation of slightly different hole sizes in electrohydrodynamically driven lattices (Fig. 4, A and E) and may originate from either gravity-induced symmetry breaking or a spontaneous symmetry breaking in the vertical direction (*15*). The direction of rotation of a toroid can also spontaneously change in a complicated electrohydrodynamic event that starts with a Plateau-Rayleigh–like instability along the toroid (fig. S6 and movie S16).

Although all of the presented active particles are liquid droplets, they rarely coalesce, even in close contact. This is seen in self-assemblies of droplets, wherein smaller droplets tend to localize near vertices of the polygonal droplets (Fig. 5H and movies S17 and S18). The suppressed coalescence is notably evident at high droplet concentrations and allows formation of active emulsions (Fig. 5I and movie S19). The suppressed coalescence in the self-assemblies (Fig. 5H) and in the active emulsions (Fig. 5I) arises from the electrohydrodynamic driving that leads to hydrodynamic and electrostatic forces between the droplets. These forces can be, generally, attractive or repulsive (*16*, *37*–*39*). In the case of the droplet self-assembly, a major

component of the repulsion originates likely from the electrostatic force because the electric dipoles of the rotating peak of the polygonal droplet and the satellite droplet are approximately aligned. On the other hand, in the case of the active emulsions, the electric dipolar forces can be attractive or repulsive depending on the detailed arrangement of the droplets next to each other. Thus, the suppressed coalescence between the droplets in the active emulsion likely originates from the extremely fast tangential flows on the droplet surfaces that lead to the surrounding liquid being continuously pulled into the thin gaps between the droplets. This effect is akin to the hydrodynamic lubrication and is known to be strong enough to overcome dipolar attraction in some electrohydrodynamic systems (*38*).

DISCUSSION

We have shown that an unexpected diversity of non-equilibrium states including interfacial patterns, Quincke rolling filaments, filament networks, ordered fluidic lattices, active droplets and droplets with polygonal and toroidal shapes, droplet self-assemblies, and active emulsions can emerge when driving a simple biphasic planar system out of the thermodynamic equilibrium using electrohydrodynamic shearing. We focused on a very specific case of a nonconductive fluid (PFPE), which does not wet the electrodes, surrounded by a conductive liquid (AOT/DD), which does wet the electrodes. It is expected that the observed non-equilibrium structures can be widely tuned by adjusting the liquid viscosities, conductivities, and interfacial tension (*15*). The confinement thickness also plays a role, and we observed that the instabilities and structure formation were suppressed in sample cells with considerably smaller height h than reported here. This is, at least partially, explained by the stabilizing Laplace pressure increasing with decreasing h (*30*), whereas the electric stresses remain approximately independent of the cell height if the electric field is constant (*31*).

The experiments were conducted using the electric field E_0 as the main adjustable parameter. Switching between the thermodynamic equilibrium structure and the non-equilibrium structures was performed by turning on the field nearly instantaneously. However, note that switching the structures is also possible by switching between two nonzero driving voltages or by gradually changing the driving field strength.

Many of the observed phenomena can be classified as purely driven by the external field (e.g., the 1D corrugation pattern and the 2D liquid lattices), while some are also clearly of active nature (e.g., the Quincke rolling droplets). There are also phenomena that evade the straightforward categorization to "driven" or "active" (e.g., the Quincke rolling filaments and the dense emulsion of droplets). Thus, the presented system shows that switching between driven and active behavior is possible in a single system, also highlighting that the transition from the driven state to the emergence of activity can be complex.

We foresee that the exceptionally rich dynamics of the system will open several new avenues in many fields of research. In the field of EHD, the plethora of non-equilibrium structures in the specific system of liquids presented here points toward the avenue of discovering many other unexpected dissipative structures by adjusting the fluid properties, especially the viscosity and conductivity that are known to lead to highly nontrivial behaviors in nonconfined droplets (*15*), including equatorial streaming (*25*) and dimpling (*40*). In addition, the three-phase contact angle and the confinement height emerge as new control parameters that remain largely unexplored in the field of EHD (*15*, *27*). In the field of capillary phenomena, the quasi-stationary polygonal droplets go beyond the known pulsating polygonal and star-shaped droplets (*26*, *41*) and, together with the energetically highly unfavorable filaments with large surface areas, pave way toward wider exploration of non-equilibrium droplet shapes driven by electrohydrodynamic or other mechanisms (*30*). In the field of pattern formation, the 1D interfacial pattern and the 2D fluidic lattices contribute to the known externally driven dissipative patterns (*1*), pointing toward the need for a thorough theoretical and experimental analysis of the possible biphasic lattice geometries, and also the transitions between the well-ordered lattices and the fluctuating random filament networks coexisting with the lattices (movie S7). In the field of dissipative self-assembly (*2*), our results suggest that electrohydrodynamic can be used to assemble objects in programmable locations along larger structures (Fig. 5H) to create hierarchical dissipative self-assemblies (*42*). In the field of active particle physics, the liquid Quincke rollers allow an exciting new approach to collective states of active rollers previously studied using solid particles (*16*–*18*). The liquid droplets exhibit interparticle interactions that are a function of the droplet viscosity (*43*), allowing on-the-fly control of the interactions by adjusting the viscosity, as well as on-demand creation of the roller populations from a larger reservoir. Last, in the field of active emulsions, our results show that EHD can be used for both creating and stabilizing emulsions (*25*, *44*, *45*) that can be directly visualized thanks to the well-defined 2D confinement, with the dynamics of the emulsion compared to other active emulsions that have been, so far, mostly envisioned and realizing using non-equilibrium chemical reactions (*46*, *47*).

On the technological side, the biphasic system studied here offers exciting possibilities as optical devices because of the exceptional control over the liquid-liquid interface and fluidic structures with electric field. This will immediately lead to technologically relevant voltage-controlled non-equilibrium optical diffusers and structural colors based on photonic crystals and glasses by controlling the formation, interactions, and self-assembly of the various fluidic structures demonstrated here.

MATERIALS AND METHODS

Materials

n-Dodecane (99%, anhydrous, Acros Organics), PFPE (Krytox GPL 102-500, Chemours Performance Lubricants), docusate sodium salt (AOT, ≥99%, anhydrous, Sigma-Aldrich), and glass slides coated with ITO and silver contact strips (75 mm by 25 mm by 1 mm, nominal coating thickness of ca. 350 nm; Diamonds Coatings Ltd.) were used as obtained from the manufacturer. Thermoplastic ionomer spacer film was custom-made from ionomer granules (Surlyn 1702, DuPont, Finland) by Muovipoli Oy (Finland). All materials were handled under ambient laboratory conditions (temperature $T \approx 22$°C, relative humidity between 12 and 18%). The leaky dielectric solution (AOT/DD) with a nominal concentration of 150 mM was prepared by mixing 3.34 g of AOT and 48.41 ml of DD. The AOT dissolved completely without any agitation in approximately 4 hours. Solution (75 mM) was prepared by mixing 1 ml of the 150 mM solution with 1 ml of *n*-dodecane.

Visualization of contact angles and adhesion

The contact angles and adhesion of PFPE on the ITO surface were visualized using an optical goniometer (Biolin Scientific Attension

Theta). A small piece of ITO-coated glass slide (ca. 9.5 mm by 9.5 mm by 1 mm) was cut using a diamond glass cutter and placed at the bottom of a glass cuvette (45 mm by 10 mm by 10 mm; Hellma Analytics), with the ITO-coated surface facing upward. The cuvette was then half-filled with the AOT/DD solution. PFPE droplets were manually dispensed using a 1-ml syringe (Hanke Sass Wolf GmbH) and a needle (nominal outer diameter φ_o = 0.72 mm and nominal inner diameter φ_i = 0.41 mm; Hamilton Bonaduz, Kel-F hub needles) mounted on the goniometer.

Measurements of oil densities

The densities of the 150 mM AOT in DD solution and PFPE (table S3) were measured by aspirating 100 µl of each liquid with a positive displacement pipette (Eppendorf Multipette E3x) and measuring the mass of the aspirated liquid using an analytical balance (Ohaus Pioneer).

Determination of interfacial tension

The interfacial tension was determined using the pendant drop method, using the same setup used for visualization of contact angles and adhesion, with the exception that the needle was kept far from the ITO-coated glass slide. An image of a PFPE droplet hanging steadily was analyzed using the goniometer software (Biolin Scientific OneAttension), using measured liquid densities (table S3).

Planar sample cell construction

Each planar sample cell (Hele-Shaw cell) was constructed from two pristine ITO-coated glass slides and a Surlyn spacer. A square opening of ca. 1 cm by 1 cm was cut using a razor blade along one side of the rectangular spacer film of ca. 4 cm by 2.5 cm. The spacer film was placed between the ITO slides and briefly melted by placing the cell on a hotplate (Thermo Fisher Scientific) at 100°C for 10 min, with a small weight of 20 to 30 g on top of the cell. Upon cooling, the molten spacer film adheres strongly to the ITO-coated glass slides, resulting in a robust cell that can hold approximately 6.5 µl of liquid in square planar confinement with height of ca. 65 µm (fig. S1A). Three sides of the confinement are formed by the spacer film; the fourth is open to air and is used to fill the sample with the biphasic system.

Determination of the sample cell thickness

The sample cell thickness was determined using a homemade white light interferometer constructed from a white light-emitting diode (LED; Thorlabs, MWWHF2) connected to a fiber optic reflection probe bundle (Thorlabs, RP22), passing the light to the sample and also collecting the reflected light and passing it to a spectrometer (Thorlabs, CCS100/M). This setup was operated using the software provided by the manufacturer (Thorlabs OSA). The cell height h was determined from the interference spectrum as

$$h = \frac{\lambda_p \lambda_0}{2n(\lambda_p - \lambda_0)}$$

where λ_0 is the wavelength of one (arbitrary, 0th) interference peak, λ_p is the wavelength of the pth peak after the 0th peak, and n is the refractive index of the medium (air) (*48*). The heights of all sample cells used here (table S1) are averages of nine measurements per cell from different locations (fig. S1B). The variability of cell thickness within one cell was characterized as the SD of the nine measurements and varied from approximately 0.2 to 0.9 µm.

Measurements of oil conductivities

Oil conductivities (table S3) were measured in the planar cells by pipetting a small volume of each oil into a planar cell, followed by application of a DC voltage of U = 100 V and measurement of the resulting current I using a sourcing electrometer (Keysight, B2987A). The conductivity was calculated as $\sigma = hI/AU$, where A is the area occupied by the oil in the cell, determined using image analysis (ImageJ) from an acquired image of the filled cell. The conductivity of the spacer material was assumed to be negligible.

Optical microscopy under electrohydrodynamic shearing

The sample cells were filled using capillary action by placing the tip of an oil-filled pipette (10 µl; Eppendorf Research plus) near the open side of the cell. First, 50 to 70% of the cell volume were filled with the AOT/DD solution, and then the remaining 30 to 50% were filled with PFPE.

The filled cell was observed using a modular homemade microscopy setup with transmitted light illumination, allowing the use of various magnifications and imaging speeds. Briefly, the main components of the system include optomechanical components (Thorlabs), an infinity-corrected objective lens (Nikon 1×/0.04, 5×/0.15, 10×/0.30, 20×/0.45, or 50×/0.80), a tube lens (Thorlabs) or a finite-conjugate low-magnification zoom lens (Edmund Optics VZM 450, 0.75× to 4.5×), a USB3 camera (PointGray Grasshopper GS3-U3-51S5M-C, 2448 × 2048 at 75 fps) or a high-speed camera (Phantom Miro M310, 1280 × 800 at 3200 fps), and a collimated light source (Thorlabs, MWWHLP1 LED coupled to SM2F32-A collimator). The magnification and length scale of the images were calibrated using a calibration target (Thorlabs, R1L3S2P). The DC electric field was applied to the sample using the sourcing electrometer (Keysight, B2987A) and hookup wires rated to 600 V (Alpha Wire, 2936). Wires were attached to the silver contact bars on the ITO slides with small magnets. The cameras and electrometer were operated using their manufacturers' software. See table S2 for a complete list of experimental conditions for each experiment presented here.

We note that, despite the large driving voltages, the electric current in the samples is small, typically close to 100 µA at maximum driving voltages of several hundreds of volts. This leads to only a few tens of milliwatts of heating power, which is not sufficient to notably increase the sample temperature during the experiments.

Image processing and analysis

Native gamma and contrast settings were used for images produced by the two cameras. For images taken with the PointGray camera, the gamma is 1.0. For images taken with the Phantom camera, the gamma is 2.2. Contrast enhancement using histogram adjustment (ImageJ) was performed only for images shown in fig. S5B. The interface elongation (Fig. 2A) was captured using the PointGray Grasshopper GS3-U3-51S5M-C at 50 fps. The image intensity along the axis perpendicular to the interface was determined using the Profile function of ImageJ and by averaging more than 30 neighboring lines of pixels. Full width at half maximum (FWHM) of the intensity profile was obtained with a custom MATLAB script for each time point (Fig. 2C). Final reported values (Fig. 2B) are values averaged over time.

SUPPLEMENTARY MATERIALS

Supplementary material for this article is available at https://science.org/doi/10.1126/sciadv.abh1642

REFERENCES AND NOTES

1. M. Cross, H. Greenside, *Pattern Formation and Dynamics in Nonequilibrium Systems* (Cambridge Univ. Press, 2009).
2. G. M. Whitesides, B. Grzybowski, Self-assembly at all scales. *Science* **295**, 2418–2421 (2002).
3. M. C. Marchetti, J. F. Joanny, S. Ramaswamy, T. B. Liverpool, J. Prost, M. Rao, R. A. Simha, Hydrodynamics of soft active matter. *Rev. Mod. Phys.* **85**, 1143–1189 (2013).
4. B. A. Grzybowski, H. A. Stone, G. M. Whitesides, Dynamic self-assembly of magnetized, millimetre-sized objects rotating at a liquid–air interface. *Nature* **405**, 1033–1036 (2000).
5. J. Palacci, S. Sacanna, A. P. Steinberg, D. J. Pine, P. M. Chaikin, Living crystals of light-activated colloidal surfers. *Science* **339**, 936–940 (2013).
6. J. Prost, F. Jülicher, J.-F. Joanny, Active gel physics. *Nat. Phys.* **11**, 111–117 (2015).
7. F. J. Ndlec, T. Surrey, A. C. Maggs, S. Leibler, Self-organization of microtubules and motors. *Nature* **389**, 305–308 (1997).
8. J. Boekhoven, W. E. Hendriksen, G. J. M. Koper, R. Eelkema, J. H. van Esch, Transient assembly of active materials fueled by a chemical reaction. *Science* **349**, 1075–1079 (2015).
9. S. A. P. van Rossum, M. Tena-Solsona, J. H. van Esch, R. Eelkema, J. Boekhoven, Dissipative out-of-equilibrium assembly of man-made supramolecular materials. *Chem. Soc. Rev.* **46**, 5519–5535 (2017).
10. S. De, R. Klajn, Dissipative self-assembly driven by the consumption of chemical fuels. *Adv. Mater.* **30**, 1706750 (2018).
11. J. Jhawar, R. G. Morris, U. R. Amith-Kumar, M. Danny Raj, T. Rogers, H. Rajendran, V. Guttal, Noise-induced schooling of fish. *Nat. Phys.* **16**, 488–493 (2020).
12. I. D. Couzin, J. Krause, in *Advances in the Study of Behavior* (Academic Press, 2003), vol. 32, pp. 1–75.
13. M. Fialkowski, K. J. M. Bishop, R. Klajn, S. K. Smoukov, C. J. Campbell, B. A. Grzybowski, Principles and implementations of dissipative (dynamic) self-assembly. *J. Phys. Chem. B* **110**, 2482–2496 (2006).
14. É. Fodor, C. Nardini, M. E. Cates, J. Tailleur, P. Visco, F. van Wijland, How far from equilibrium is active matter? *Phys. Rev. Lett.* **117**, 038103 (2016).
15. P. M. Vlahovska, Electrohydrodynamics of drops and vesicles. *Annu. Rev. Fluid Mech.* **51**, 305–330 (2019).
16. A. Bricard, J.-B. Caussin, N. Desreumaux, O. Dauchot, D. Bartolo, Emergence of macroscopic directed motion in populations of motile colloids. *Nature* **503**, 95–98 (2013).
17. A. Bricard, J.-B. Caussin, D. Das, C. Savoie, V. Chikkadi, K. Shitara, O. Chepizhko, F. Peruani, D. Saintillan, D. Bartolo, Emergent vortices in populations of colloidal rollers. *Nat. Commun.* **6**, 7470 (2015).
18. A. Morin, N. Desreumaux, J.-B. Caussin, D. Bartolo, Distortion and destruction of colloidal flocks in disordered environments. *Nat. Phys.* **13**, 63–67 (2017).
19. Z. Rozynek, A. Mikkelsen, P. Dommersnes, J. O. Fossum, Electroformation of Janus and patchy capsules. *Nat. Commun.* **5**, 3945 (2014).
20. P. Dommersnes, Z. Rozynek, A. Mikkelsen, R. Castberg, K. Kjerstad, K. Hersvik, J. Otto Fossum, Active structuring of colloidal armour on liquid drops. *Nat. Commun.* **4**, 2066 (2013).
21. M. Ouriemi, P. M. Vlahovska, Electrohydrodynamics of particle-covered drops. *J. Fluid Mech.* **751**, 106–120 (2014).
22. M. Ouriemi, P. M. Vlahovska, Electrohydrodynamic deformation and rotation of a particle-coated drop. *Langmuir* **31**, 6298–6305 (2015).
23. P. F. Salipante, P. M. Vlahovska, Electrohydrodynamics of drops in strong uniform dc electric fields. *Phys. Fluids* **22**, 112110 (2010).
24. P. M. Vlahovska, Electrohydrodynamic instabilities of viscous drops. *Phys. Rev. Fluids* **1**, 060504 (2016).
25. Q. Brosseau, P. M. Vlahovska, Streaming from the equator of a drop in an external electric field. *Phys. Rev. Lett.* **119**, 034501 (2017).
26. A. Varshney, S. Ghosh, S. Bhattacharya, A. Yethiraj, Self organization of exotic oil-in-oil phases driven by tunable electrohydrodynamics. *Sci. Rep.* **2**, 738 (2012).
27. S. K. Tadavani, J. R. Munroe, A. Yethiraj, The effect of confinement on the electrohydrodynamic behavior of droplets in a microfluidic oil-in-oil emulsion. *Soft Matter* **12**, 9246–9255 (2016).
28. R. Großmann, I. S. Aranson, F. Peruani, A particle-field approach bridges phase separation and collective motion in active matter. *Nat. Commun.* **11**, 5365 (2020).
29. J. V. I. Timonen, M. Latikka, L. Leibler, R. H. A. Ras, O. Ikkala, Switchable static and dynamic self-assembly of magnetic droplets on superhydrophobic surfaces. *Science* **341**, 253–257 (2013).
30. P.-G. de Gennes, F. Brochard-Wyart, D. Quere, *Capillarity and Wetting Phenomena: Drops, Bubbles, Pearls, Waves* (Springer, ed. 2004, 2003).
31. G. I. Taylor, A. D. McEwan, L. N. J. de Jong, Studies in electrohydrodynamics. I. The circulation produced in a drop by an electric field. *Proc. R. Soc. Lond. A* **291**, 159–166 (1966).
32. M.-T. Westra, D. J. Binks, W. V. D. Water, Patterns of Faraday waves. *J. Fluid Mech.* **496**, 1–32 (2003).
33. R. E. Rosensweig, *Ferrohydrodynamics* (Dover Publications, 2014).
34. G. Quincke, Ueber Rotationen im constanten electrischen Felde. *Ann. Phys.* **295**, 417–486 (1896).
35. G. E. Pradillo, H. Karani, P. M. Vlahovska, Quincke rotor dynamics in confinement: Rolling and hovering. *Soft Matter* **15**, 6564–6570 (2019).
36. J. Eggers, Nonlinear dynamics and breakup of free-surface flows. *Rev. Mod. Phys.* **69**, 865–930 (1997).
37. D. Das, D. Saintillan, Electrohydrodynamic interaction of spherical particles under Quincke rotation. *Phys. Rev. E* **87**, 043014 (2013).
38. P. Dommersnes, A. Mikkelsen, J. O. Fossum, Electro-hydrodynamic propulsion of counter-rotating Pickering drops. *Eur. Phys. J. Spec. Top.* **225**, 699–706 (2016).
39. J. C. Baygents, N. J. Rivette, H. A. Stone, Electrohydrodynamic deformation and interaction of drop pairs. *J. Fluid Mech.* **368**, 359–375 (1998).
40. B. W. Wagoner, P. M. Vlahovska, M. T. Harris, O. A. Basaran, Electric-field-induced transitions from spherical to discocyte and lens-shaped drops. *J. Fluid Mech.* **904**, R4 (2020).
41. X. Ma, J.-J. Liétor-Santos, J. C. Burton, Star-shaped oscillations of Leidenfrost drops. *Phys. Rev. Fluids* **2**, 031602 (2017).
42. Y. Alapan, B. Yigit, O. Beker, A. F. Demirörs, M. Sitti, Shape-encoded dynamic assembly of mobile micromachines. *Nat. Mater.* **18**, 1244–1251 (2019).
43. S. Santra, D. Sen, S. Das, S. Chakraborty, Electrohydrodynamic interaction between droplet pairs in a confined shear flow. *Phys. Fluids* **31**, 032005 (2019).
44. K. Ho Lee, M. Ireland, B. L. Miller, B. E. Wyslouzil, J. O. Winter, Synthesis of polymer nanoparticles via electrohydrodynamic emulsification-mediated self-assembly. *J. Colloid Interface Sci.* **586**, 445–456 (2021).
45. Y. S. Song, Y. H. Choi, D. H. Kim, Microextraction in a tetrabutylammonium bromide/ammonium sulfate aqueous two-phase system and electrohydrodynamic generation of a micro-droplet. *J. Chromatogr. A* **1162**, 180–186 (2007).
46. C. A. Weber, D. Zwicker, F. Jülicher, C. F. Lee, Physics of active emulsions. *Rep. Prog. Phys.* **82**, 064601 (2019).
47. J. Ignés-Mullol, F. Sagués, Active, self-motile, and driven emulsions. *Curr. Opin. Colloid Interface Sci.* **49**, 16–26 (2020).
48. T. H. Besseling, J. Jose, A. V. Blaaderen, Methods to calibrate and scale axial distances in confocal microscopy as a function of refractive index. *J. Microsc.* **257**, 142–150 (2015).

Acknowledgments

Funding: This work is supported by Academy of Finland 316219 (to J.V.I.T.) and European Research Council 803937 (to J.V.I.T.). **Author contributions:** Conceptualization: J.V.I.T. Experimental work: G.R. Data analysis and interpretation: G.R., N.K., and J.V.I.T. Visualization: G.R. and J.V.I.T. Supervision: J.V.I.T. Writing (original draft): G.R. and N.K. Writing (review and editing): G.R., N.K., and J.V.I.T. **Competing interests:** The authors declare that they have no competing interests. **Data and materials availability:** All data needed to evaluate the conclusions in the paper are present in the paper and/or the Supplementary Materials. High-resolution uncompressed video data and the analysis codes are available in the Zenodo repository (DOI: 10.5281/zenodo.4889182).

Submitted 4 March 2021
Accepted 23 July 2021
Published 15 September 2021
10.1126/sciadv.abh1642

Citation: G. Raju, N. Kyriakopoulos, J. V. I. Timonen, Diversity of non-equilibrium patterns and emergence of activity in confined electrohydrodynamically driven liquids. *Sci. Adv.* **7**, eabh1642 (2021).

ScienceAdvances

Diversity of non-equilibrium patterns and emergence of activity in confined electrohydrodynamically driven liquids

Geet RajuNikos KyriakopoulosJaakko V. I. Timonen

Sci. Adv., 7 (38), eabh1642. • DOI: 10.1126/sciadv.abh1642